Wiley Analytical Science

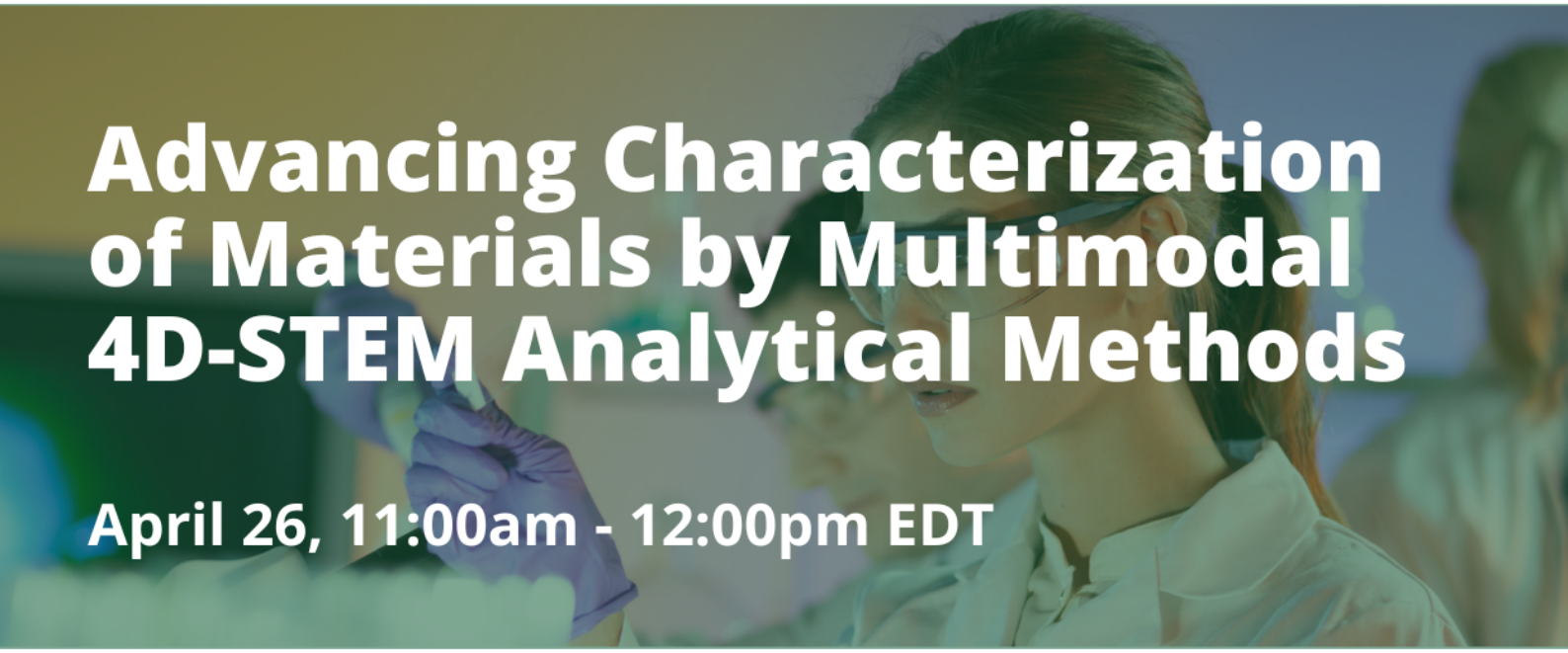

Advancing Characterization of Materials by Multimodal 4D-STEM Analytical Methods

April 26, 11:00am - 12:00pm EDT

Development and production of new materials and semiconductor devices require morphological, structural, and chemical characterization at the nanoscale level to understand their chemico-physical properties and optimize their production process. Besides traditional electron microscopy imaging and compositional analysis techniques, 4D-STEM methods provide additional structural information about the local internal organization of atoms and molecules at each position of an acquired STEM map.

Watch this session during the WAS Virtual Conference:

Dr. Daniel Nemecek

Dr. Tingting Yang

Register Now

This talk is sponsored by TESCAN
PERFORMANCE IN NANOSPACE

ADVANCED OPTICAL MATERIALS
www.advopticalmat.de

Engineering Fano-Resonant Hybrid Metastructures with Ultra-High Sensing Performances

Giuseppe Emanuele Lio, Antonio Ferraro, Rafał Kowerdziej, Alexander O. Govorov, Zhiming Wang,* and Roberto Caputo**

Metamaterials-based sensors are of primary interest in physics, materials science, medicine, and biophysics thanks to their ability to detect very tiny amount of molecules spread into a medium. Here, a metastructure utilizing the epsilon near zero (ε_{NZ}) and Fano–Rabi physics is engineered to design a system with ultra-high sensitivity. So far, a dedicated study of such systems has been missing. In this work, the authors report the results of their efforts to fill the gap by considering a metasurface, designed as a periodical array of rings with a cross in their center, placed on top of a silver (Ag) and zinc oxide (ZnO) epsilon near-zero optical nanocavity (ε_{NZ}-ONC) metamaterial. The accurate selection of the metasurface parameters allows the design of a sensor exhibiting an extremely high sensitivity of about 16 000 and 21 000 nm RIU^{-1} depending on incoming polarization. This work paves the way for the development of novel groundbreaking devices for biomedical and environmental application based on plasmonic and photonic design principles.

1. Introduction

In recent years, the design and realization of bio-sensors based on plasmonic/nanophotonic structures is spurring unprecedented interest as diagnostic protocol for cancer and infectious diseases.[1–3] Significant efforts have been devoted to design photonic structures at the nano-scale for probing genes and proteins bound to specific receptors.[4–6] In this scenario, an important role is played by the combination of metamaterials and metasurfaces into metastructures showing intriguing functionalities. The first ones represent a particular family of man-made materials exhibiting peculiar physical properties not directly found in nature, whereas the second ones produce peculiar photonic functionalities when light passes their sub-wavelength thickness. The physics behind these coupled systems finds its grounds in the interaction between resonances (plasmonic/confined modes) and Rayleigh anomalies.[7–9] In the specific case, metasurfaces can support Fano–Feshbach resonances (FFRs) generating line-shapes identical to those usually associated to electromagnetically induced transparency (EIT).[10–14]

FFRs occur as interference between two scattering waves, one related to the bulk interaction (continuum states) and one due to the excitation of a discrete state corresponding to the resonant process. FFRs are manifested in the absorption cross section, $\sigma(\hbar\omega)$, described by the Fano formula

$$\sigma(\hbar\omega) = D^2((q+\Omega)^2)/(1+\Omega^2) \quad (1)$$

G. E. Lio
Physics Department
University of Florence
Via Sansone 6, Sesto Fiorentino, (FI) 50019, Italy

G. E. Lio
European Laboratory for Non Linear Spectroscopy (LENS)
Via Nello Carrara 1, Sesto Fiorentino, (FI) 50019, Italy

A. Ferraro, R. Caputo
Consiglio Nazionale delle Ricerche - Istituto di Nanotecnologia (CNR-Nanotec)
via P. Bucci cubo 33c, Rende, CS 87036, Italy
E-mail: roberto.caputo@unical.it

The ORCID identification number(s) for the author(s) of this article can be found under https://doi.org/10.1002/adom.202203123.

DOI: 10.1002/adom.202203123

R. Kowerdziej
Institute of Applied Physics
Military University of Technology
2 Kaliskiego St., Warsaw 00-908, Poland

A. O. Govorov
Department of Physics and Astronomy
Ohio University
Athens, OH 45701, USA
E-mail: govorov@ohio.edu

Z. Wang, R. Caputo
Institute of Fundamental and Frontier Sciences
University of Electronic Science and Technology of China
Chengdu 610054, China
E-mail: zhmwang@uestc.edu.cn

Z. Wang
Institute for Advanced Study
Chengdu University
Chengdu 610106, China

R. Caputo
Physics Department
University of Calabria
via P. Bucci cubo 31c, Rende, CS 87036, Italy

where $\hbar\omega$ is the photon energy and $q = \cot\delta$ is the Fano parameter that specifies the ratio of the resonant absorption (due to the metastructure) to the direct absorption amplitude (due to the bare substrate), δ is the phase shift deriving from the interaction of light with metallic slabs, $\Omega = 2(\hbar\omega - \hbar\omega_0)/\Gamma$, where Γ and $\hbar\omega_0$ are respectively width and energy of the given resonance and $D^2 = 4\sin 2\delta$.[15–17] The Fano formula is generally applicable to the considered optical spectral range in a variety of metastructure systems.[18] The FFR spectral location and line-shape are determined by the geometry (periodicity and unit-cell features) of the metasurface placed on top of the considered plasmonic system.[7] The latter can be constituted by optical nano-cavities (ONC) exhibiting epsilon near-zero (ε_{NZ}) behavior with giant phase shift (δ).[12,13,19,20] The ε_{NZ} system guarantees the existence of two distinct surface plasmon polariton (SPP) modes (at the top or at the bottom of the metal–insulator interfaces[21]), with different k-vectors at the resonant wavelengths, that can merge into a coupled state also known as gap surface plasmon (GSP) which has its own resonant wavelength ($\lambda_{\varepsilon_{NZ}}$-ONC[22]). If the typical periodicity of the unit metasurface element P (**Figure 1**a) is such that the related lattice resonance is nearly close to the ε_{NZ}-ONC one, the line-shape can show a narrow feature, which is a consequence of the losses in the metal layers.[23]

2. Results and Discussions

The intriguing challenge of the proposed work is to study the optical behavior of a polymeric metasurface, designed as a periodical displacement of rings with a cross in their centers, placed on top of an ε_{NZ}-ONC. Figure 1a reports a sketch of the designed system where $P = Px = Py$ is the period of the metasurface, W_c the cross arm length, W_e and W_i represent the outer and inner radii of the ring, respectively. Starting from the glass substrate, the considered ε_{NZ}-ONC comprises of a silver (Ag) layer of 30 nm and a thick zinc oxide (ZnO) cavity of 160 nm followed by other 30 nm layers of Ag and 20 nm of ZnO where the cavity thickness plays a fundamental role to determine the confined modes propagating within the metamaterial.[19,22] As addressed in our previous works,[13,24] for the selected t_{cav} = 160 nm, two confined modes appear, that is, $m = 0$ and $m = 1$, centered respectively at $\lambda_0 \approx 405$ nm and $\lambda_1 \approx 780$ nm. The fact that this ONC supports a double plasmonic mode, at lower and higher energies, means that interface interactions with bound and anti-bound modes are allowed.[25] The proposed coupled system is numerically investigated by means of a suitable "Reticolo" script[26] which exploits the rigorous coupled wave analysis (RCWA), details are available in the Experimental Section whereas some sample codes are reported in Section S2, Supporting Information. The refractive indices of the materials used for the simulation are reported in Figure S1, Supporting Information. In order to design optimized metastructures, we have to consider at least two main aspects: first, we span the entire visible range and second, the metasurface has to interact with the plasmonic resonances of the ε_{NZ}-ONC. To this end, the presented metasurface is a periodic structure whose unit cell is chosen as a cross centered into a ring (Figure 1a) with thickness fixed at 300 nm, thus ensuring a subwavelength behavior for almost the whole considered spectral range. A general perspective of the metastructure optical response can be caught by performing a parametric sweep study in which the period P of the unit cell is varied from 100 to 1000 nm with 4 nm steps and the fill fraction is fixed at 67%. The structure parameters are accordingly calculated as a function of P following the formulas

$$W_e = (P/2)\times 1.45 \quad (2)$$

$$W_i = (P/2)\times 0.85 \quad (3)$$

$$W_c = (P/4) \quad (4)$$

The obtained reflectance (R) and absorbance (A) maps, reported in Figure 1b,c, suggest that a dip in reflectance corresponds to a peak in absorbance in agreement with the Fano description. An insight of these results is reported in **Figure 2**a,b where the stacked plots (with 50 nm steps) clearly evidence the presence of FFR and Rabi-analogue splits[27] which strongly depend on the geometrical parameters of the metasurface; numbers (1–8) identify the different spectral behaviors shown in the maps and explained hereafter.

Three Rabi-analogue splits (anti-crossing modes) are observed for periods spanning from ≈100 nm to ≈600 nm. In this range, when R goes to zero, A increases (up to case # 5). The opposite situation occurs when the period changes from 700 nm to 1000 nm (case # 6 – # 8), which is the case for shorter wavelengths. This

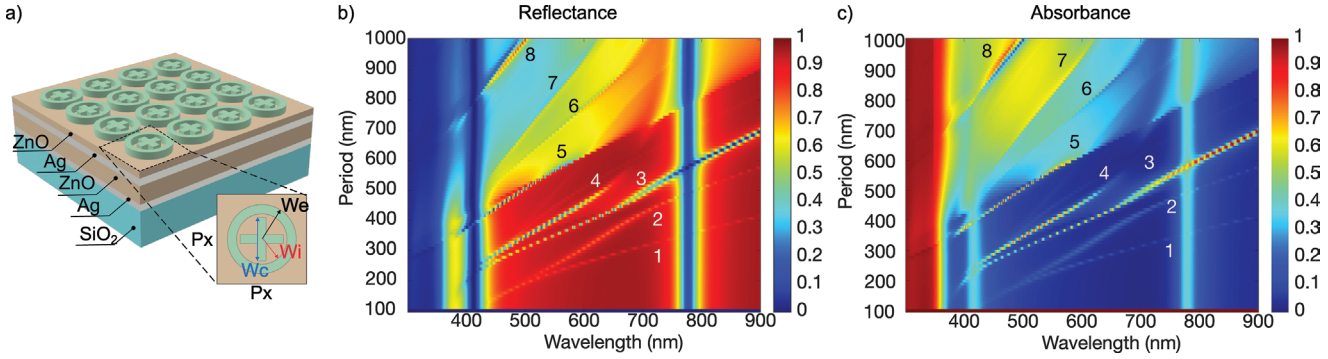

Figure 1. a) Schematic sketch of the proposed metastructure where $P = P_x = P_y$ is the period of the metasurface, W_c the cross arm length, W_e and W_i are the external and inner radius of the rings, respectively. b,c) Reflectance and absorbance maps calculated by varying the geometrical parameters as a function of the lattice period, as indicated by Equations (2)–(4). The numbers (1)–(8) identify the different spectral behaviors evidenced in the plots.

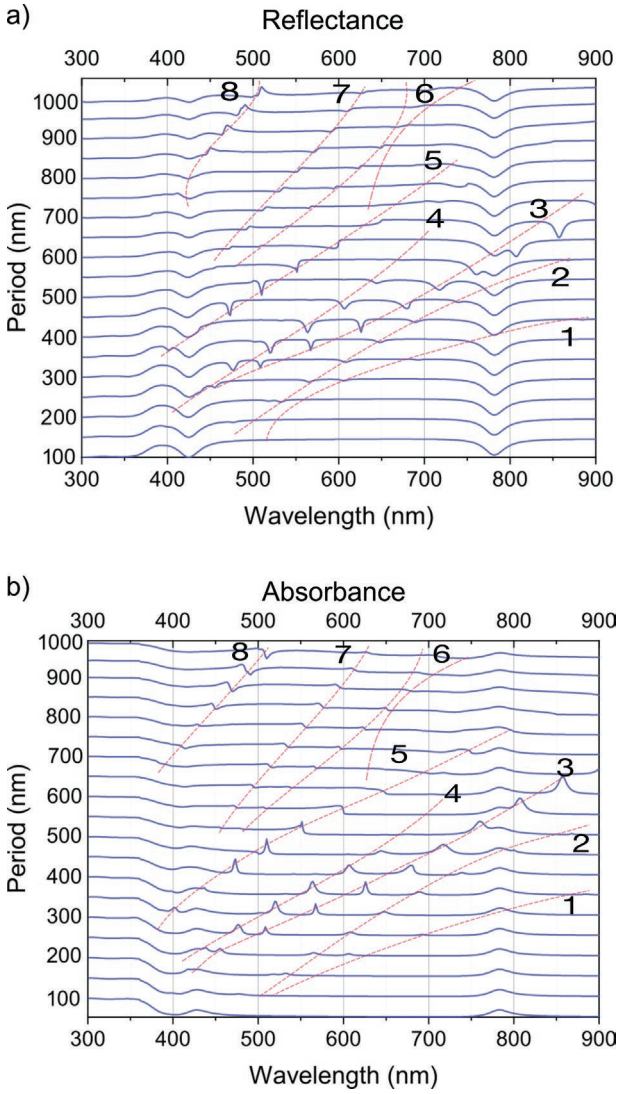

Figure 2. a,b) Stacked plots of reflectance and absorbance reported as a function of the period from 100 to 1000 nm with 50 nm steps. Numbers (1)–(8) identify the different spectral behavior shown in the plots.

is due to the presence of the FFR which is a consequence of the high wave vector (k) mode coupling induced by the metasurface placed on top of the ε_{NZ}-ONC. The stacked plots also allow an eye-catching identification of the cavity modes: indeed, the modes where R goes to zero and A is maximized, and viceversa, the modes where R is maximized and A goes to zero.

An in-depth investigation of the above-mentioned two peculiar behaviors is presented as well. For this, two sets of metasurface parameters are selected. In the first case, a period $P_x = P_y = 400$ nm is chosen that corresponds to $W_e = 290$ nm, $W_i = 170$ nm, and $W_c = 100$ nm. When the metasurface is placed on top of the ε_{NZ}-ONC, the light–matter interaction produces p-polarized R dips and A peaks at the wavelengths $\lambda = 422$, 557, 626, 689, and 781 nm, as shown in **Figure 3**a. The electric field behavior of the p-polarized coupled resonant mode at $\lambda = 626$ nm is studied by considering the refractive index modulation of the metasurface (Figure 3b(1)). As expected by the interaction of the metasurface with the ε_{NZ}-ONC, the electric field along X is highly confined between neighbor rings and in-plane coupled modes also arise between the metasurface and the cavity, as shown in Figure 3b(2). On the other hand, a highly confined electric field in the Y direction is present within the ONC, as shown in Figure 3b(3).[13] The electric field along Z presents a weak interaction among the lower Ag layer and the ZnO cavity and a strong interaction between the upper ZnO layer and the polymer structures (Figure 3b(4)). In Figure 3c, the top view of the electric field evidences the interaction of the neighboring rings. By considering the second metastructure with period increased to $P_x = P_y =$ 900 nm (and $W_e = 652$ nm, $W_i = 382$ nm, and $W_c = 225$ nm) p-polarized R peaks and A dips show up at $\lambda = 463$, 506, 591, and 669 nm, or the opposite behavior with R dips and A peaks at $\lambda = 470$, 509, 600, and 683 nm, see **Figure 4**a. The electric field simulation using p-polarized incoming radiation are now performed at $\lambda = 463$ nm. The refractive index modulation of the studied metastructure is reported in Figure 4b(1). The electric field along X is confined both inside and outside the metastructure (Figure 4b(2)), while along Y and Z it is vertically coupled with the ε_{NZ}-ONC demonstrating the presence of Fano resonances[28] (Figure 4b(3),b(4), respectively). Finally, in Figure 4c, the top view of the electric

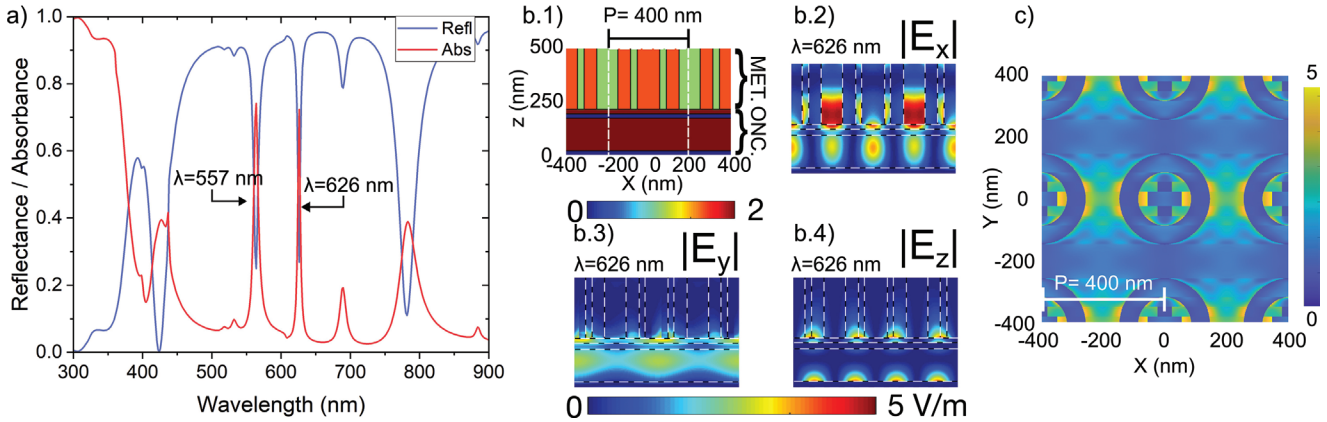

Figure 3. a) Reflectance and absorbance spectra for λ varying from 300 to 900 nm have been obtained for structures with $P_x = P_y = 400$ nm, $W_e = 290$ nm, $W_i = 170$ nm, and $W_c = 100$ nm. The metastructure exhibits two evident dips in reflectance (two peaks in absorbance) at $\lambda = 557$ nm and $\lambda = 626$ nm. b) Refractive index map displaying two unit cells of the selected geometry (1), including evaluations of the electric field at $\lambda = 626$ nm along structural sections, specifically $|E_x|$ (2), $|E_y|$ (3), and $|E_z|$ (4). c) Top-view illustration of the electric field distribution across the entire metasurface.

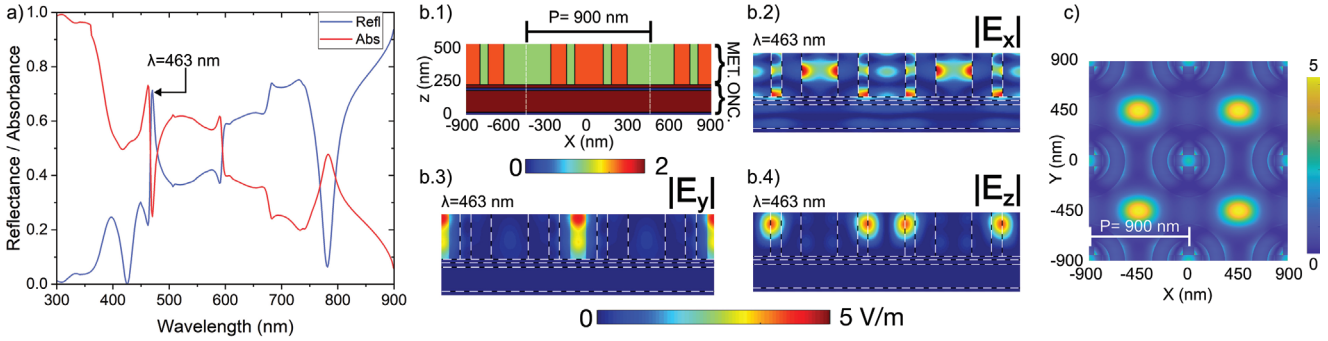

Figure 4. Reflectance and absorbance spectra for λ varying from 300 to 900 nm for the structure with $P_x = P_y = 900$ nm, $W_e = 652$ nm, $W_i = 382$ nm, and $W_c = 225$ nm. The metastructure exhibits an abrupt change in reflectance and absorbance at $\lambda = 463$ nm. b) Refractive index map displaying two unit cells of the selected geometry (1), including evaluations of the electric field at $\lambda = 463$ nm along structural sections, specifically $|E_x|$ (2), $|E_y|$ (3), and $|E_z|$ (4). c) Top-view illustration of the electric field distribution across the entire metasurface.

field highlights the confined field in the diagonal direction of neighboring unit cells.

3. Metasensor

Taking into account the observed plasmonic and Fano–Feshbach resonances, the simulated metastructure can be designed to work as a metasensor. In fact, a system able to excite FFR modes presents high performances in terms of spectral sensitivity and specificity for low molecular weight compounds such as nucleic acids, viruses, lipids, and proteins. When a particular species is dissolved in another medium like water ($\widetilde{n_{H_2O}} = 1.3330$), the initial refractive index undergoes a small variation $\tilde{n} = \widetilde{n_{H_2O}} + \delta n$ where δn represents a fingerprint of the presence of an external species in the analyzed medium. The quantity $\tilde{n} = \widetilde{n_{H_2O}} + \delta n$ is modified according with the well known procedure reported in literature.[29,30] As illustrated in **Figure 5**a, the metasensor is designed to be completely covered by the analyte through the realization of a microfluidic channel. In the corresponding simulation, we assumed that the layer of air has been replaced by a infinitely thick layer of analyte, hence, it allows retrieving the bulk sensitivity. The results obtained are therefore intended as very likely of what might be the actual experimental situation when a microfluidic channel is placed on the metastructure. The main parameters that establish the metasensor performance are the sensitivity S, calculated as the wavelength shift induced by a very small change of refractive index and measured in nm RIU^{-1}, and the spectral sensitivity $S_{\Delta\lambda}$, that is calculated as the ratio of the refractive index variation to the $\Delta\lambda$, and is measured in RIU nm^{-1}.[31] In order to evaluate the performance of the proposed metasensor, the structures constituting the metasurface are considered separately, namely first only crosses, then rings, and finally their combination. The first numerical study has been performed considering a cross unit cell and a refractive index variation from $n_{H_2O} = 1.3330$ to $\tilde{n} = 1.343$. The variation of refractive index of the metastructure overlayer from air to water has a tremendous influence on the optical response of the metastructure. In terms of *p*- and *s*-reflectance, the calculated values pass from the solid black and red lines of Figure 5 to the corresponding dashed ones. When the refractive index varies from $n_{H_2O} = 1.3330$ to $\tilde{n} = 1.343$, a red-shift from $\lambda = 546.5$ nm to $\lambda' = 548.1$ nm for R_p and from $\lambda = 619.7$ nm to $\lambda' = 621.3$ nm for R_s is observed with a spectral shift of $\Delta\lambda = 1.6$ nm for both cases. This refractive index variation ($\Delta n = 0.01$), matches a sensitivity of the system $S = 160$ nm RIU^{-1} and a spectral sensitivity $S_{\Delta\lambda} = 1.00 \times 10^{-2}$ RIU nm^{-1}, see Figure 5b. The second study considers a metasurface including only a ring as a unit cell. This time, a refractive index variation of only 0.0006 determines a wavelength shift from $\lambda = 541.8$ nm to $\lambda' = 543.3$ nm and a spectral variation of $\Delta\lambda = 1.5$ nm. This turns out into one order sensitivity increase to $S = 2500$ nm RIU^{-1} and spectral sensitivity $S_{\Delta\lambda} = 4.00 \times 10^{-4}$ RIU nm^{-1}, see Figure 5c. Finally, in the last study, the unit cell of the metasurface comprises both ring and cross, as depicted in Figure 5a. In this case, when the system is completely covered by water, a strong modification of the *p*- and *s*-pol reflectance peaks occurs which are now very sharp (black and red dashed lines in Figure 5d). In this condition, the proposed metasensor is able to resolve a refractive index variation as low as 0.0001 by producing spectral red-shifts for both light polarizations (*p*- and *s*-) from $\lambda = 476.5$ nm to $\lambda' = 478.1$ nm (*p*-pol, black and blue dashed lines respectively), and from $\lambda = 504.3.0$ nm to $\lambda' = 506.4$ nm (*s*-pol, red and purple dashed lines) as reported in Figure 5d. This turns out into an extremely high sensitivity $S^p = 16\,000$ and $S^s = 21000$ nm RIU^{-1} with a spectral sensitivity of $S^p_{\Delta\lambda} = 6.25 \times 10^{-5}$ RIU nm^{-1} and $S^s_{\Delta\lambda} = 4.76 \times 10^{-5}$ RIU nm^{-1}. The latter results are promising especially for the realization of metasensors able to detect species dissolute in different surrounding mediums.

In order to benchmark the bulk sensitivity of the proposed metasensor with that of other sensors reported in literature, relevant data has been gathered in

Table 1. Our sensor working in the visible range shows excellent performance when compared with state-of-the-art solutions. Moreover, thanks to the presence of an ε_{NZ} metamaterial, a noticeable advantage of our metasensor is that it is operated at normal incidence, for both *p*- and *s*-polarized light, and in free space thus not requiring complex optical coupling elements.

Furthermore, an in-depth numerical analysis of the robustness of the sensitivity performance has been conducted by taking into account common fabrication errors that can occur

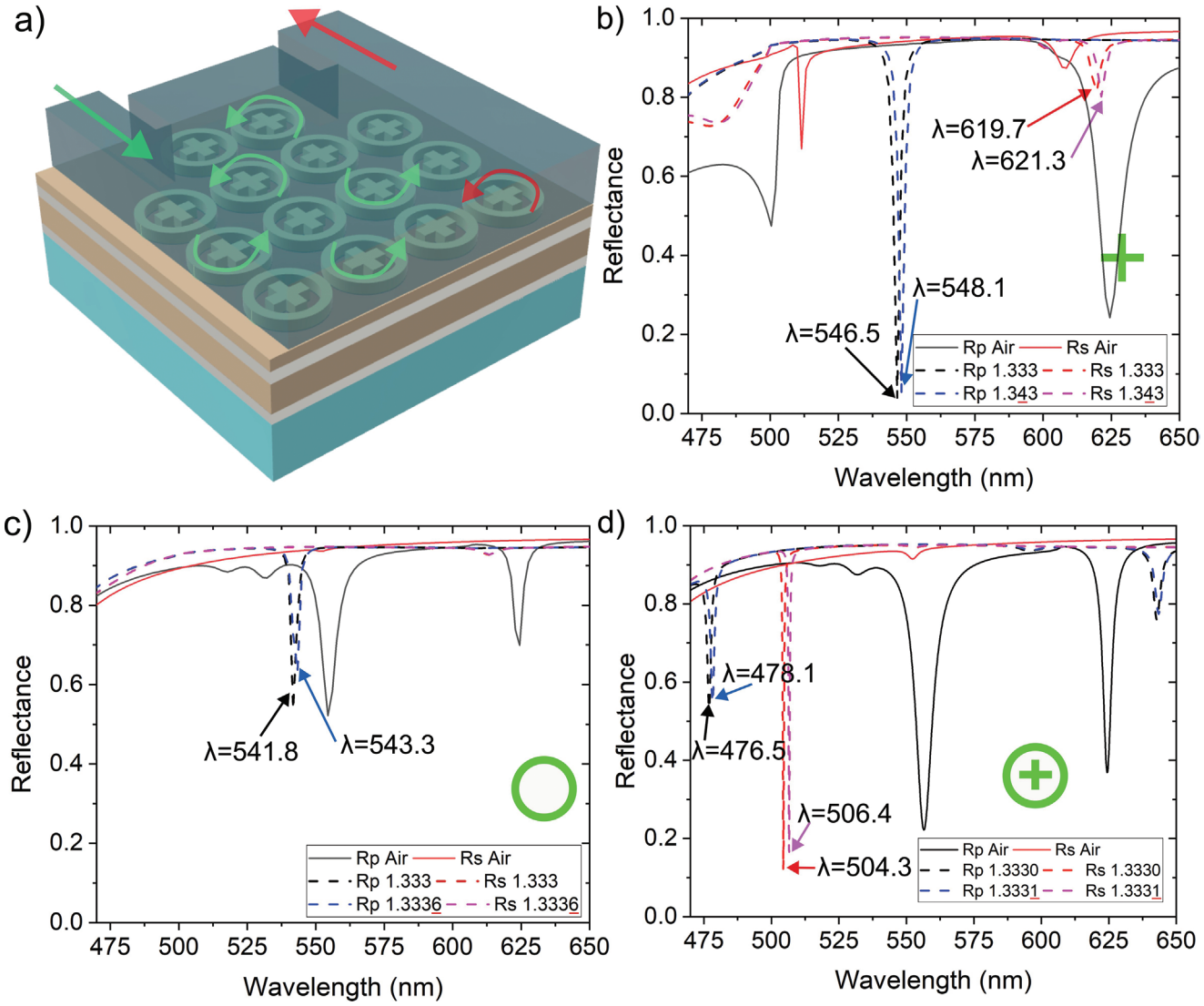

Figure 5. a) The sketch represents the micro-fluidic channel used to implement the metastructure as an ultra-high efficiency metasensor. b–d) Sensing case studies observed in air for *p*- and *s*-polarization (black and red solid lines respectively). Considering water as a surrounding medium with a refractive index of $n = 1.3330$ (blue and purple dashed lines) and with a variation of (b) $\Delta n = 0.01$, (c) $\Delta n = 0.0006$, and (d) $\Delta n = 0.0001$ showing an increasing sensitivity passing from $S = 160$ to $S = 16\,000$ nm RIU^{-1} and up to $S = 21\,000$ nm RIU^{-1} for *p*- and *s*-polarization.

during the metasurface fabrication process. Detailed information are reported in Section S3, Supporting Information.

In the first case, we considered a period fluctuation of ±20 nm in the *X* and *Y* directions in the range of 380–420 nm. As previously discussed, when the period is varied, the other parameters change accordingly (Equations (2)–(4)), as depicted in Figure S2a, Supporting Information. The results demonstrate that when the period is varied and the metastructure is covered by air, both dips in *p*- and *s*-polarization are shifted, as shown in Figure S2b, Supporting Information. By considering pure water and water with a 0.0001 refractive index variation (as shown in Figure S2c,d, Supporting Information, respectively), the sensitivity remains consistent with our previously reported results, particularly for the dips in R_s which change in the range of ±1000 nm RIU^{-1}.

In the second case, it has been analyzed the impact of variations in the cross length (W_c). We applied a ±15% variation on W_c, that results in a length change in the range of 85–115 nm, see Figure S3a, Supporting Information. Based on our previous experience in nano-fabrication,[39] we have chosen a fabrication error of ±15% for the geometrical dimensions under consideration. In this scenario, interestingly, small variations in the cross length do not significantly affect the positions of the reflectance dips in both polarizations, as depicted in Figure S3b, Supporting Information. Also in this case, the sensing performance is only slightly affected, see Figure S3c,d, Supporting Information, for both polarizations with a largest variation ±1500 nm RIU^{-1} (*p*-polarization).

In the third case, a ±15% variation on W_e and W_i is applied, resulting in a length range of 249–333 nm for W_e and 144–195 nm for W_i, see Figure S4a, Supporting Information. The results about the metastructure surrounded by air reveal that the radii variations significantly affect the position of the reflectance

Table 1. Comparative table of the present sensor with similar ones reported in literature in terms of structure type, operating wavelength and sensitivity.

Structure type	Central wavelength [nm]	Sensitivity [nm RIU^{-1}]	Year	Ref.
Hyperbolic metamaterial + nano pillar	1230	30 000	2009	[32]
Metal layer assisted guided mode resonance	809	377	2012	[33]
Halloysite nanotubes	775	10431	2018	[34]
Si3N4-based interferometric configuration	1565	1930	2019	[35]
Grating coupler to thin gold layer	1401	1133	2020	[36]
Bound state in the continuum	660	230 (close to theoretical limit)	2022	[37]
Guided mode resonance structure	1500–1770	1076	2023	[38]
Polymer metasurface on ε_{NZ}	477 (*p*-pol)	16 000		This work
Polymer metasurface on ε_{NZ}	504 (*s*-pol)	21 000		This work

dips in *p*-polarization while they do not affect the dips at all in *s*-polarization (Figure S4b, Supporting Information). When the same system is instead tested in environments with different refractive indices, such as water and water with a 0.0001 refractive index variation (Figure S4c,d, Supporting Information, respectively), the sensitivity increases by 1000 nm RIU^{-1} for both polarizations with a negative length variation (–15%) while decreases with a positive length variation (+15%).

In the fourth case, the impact of variations in the ring section has been tested. To perform this simulation, we kept fixed the inner ring radius W_i and applied a ±15% variation on the outer radius W_e, resulting in a length range of 249–333 nm, as shown in Figure S5a, Supporting Information. This scenario reveals characteristics similar to the previous cases where variations in the ring radii significantly affect the positions of the reflectance dips in *p*-polarization while in *s*-polarization they remain fixed when the metastructure is covered by air, as shown in Figure S5b, Supporting Information. The variation of sensitivity shows the same trend as in the case when both ring radii change. For all the considered fabrication errors, the Tables S1–S4, Supporting Information, report the resonance wavelengths and the corresponding values of sensitivity for the extreme variations. In all tested cases, even taking into account the worst scenario, the sensitivity remains at very high values of at least 12 000 nm RIU^{-1}, while in some situations it also increase a bit. We confidently conclude that the proposed design is very robust to fabrication error.

4. Conclusions

In conclusion, we numerically investigated the interaction of plasmonic ε_{NZ}-ONCs with an optimized polymer metasurface resulting into Fano–Feshbach resonances (FFRs) and Rabi-analogue split. These phenomenona pave the way for the realization of metasensors with extremely high performance, namely sensitivity *S* that can assume values from few hundreds to many thousands (21 000 nm RIU^{-1}). Furthermore, the proposed system presents the advantage to be excited using normally incident light thus allowing the realization of compact and portable devices, including also disposable parts that offer a quick and simple solution especially in medical applications.

5. Experimental Section

The numerical simulations were performed using a Matlab script that was based on the "Reticolo" algorithm. In the first step, the focus was on designing a metasurface coupled with an ε_{NZ} metamaterial. To find the optimal size, a code that was realized, through a "for" loop, varied the period, internal and external radius of a ring, and the length of a cross, see Example 1 in Section S1, Supporting Information. This loop returned a map of reflectance, transmittance, and absorbance (1–*T*–*R*). In the second step, once an appropriate structure was designed, the electric and magnetic fields were evaluated. For this, a part of the previous code was used and the suggested method by "Reticolo" was included to evaluate both fields. Finally, using the first code but fixing the period and structural size, tests were performed on bulk sensing by changing the medium surrounding the entire metasurface and altering the refractive index.

Materials: Silver (Ag), zinc oxide (ZnO), and soda lime glass were used as materials, with the latter serving as a substrate. Along with them, a polymeric material was also used. The refractive index of the polymer was fixed at 1.56, which is typical for a general photo-polymer, while the imaginary part is negligible.[40,41] However, the refractive indices of the other materials, which have both real and imaginary parts, were considered as a function of wavelength, as shown in Figure S1, Supporting Information.

Supporting Information

Supporting Information is available from the Wiley Online Library or from the author.

Acknowledgements

G.E.L. and A.F. contributed equally to this work. The authors acknowledge support from the bilateral (Italy-Poland) project: "Active metamaterials based on new generation liquid crystals (LCMETA)" funded by the Italian Ministry of Foreign Affairs and International Cooperation and the Polish National Agency for Academic Exchange NAWA. The publication was made with the contribution of the researcher G.E. Lio with a research

contract co-funded by the European Union—PON Research and Innovation 2014-2020 in accordance with Article 24, paragraph 3a), of Law No. 240 of December 30, 2010, as amended, and Ministerial Decree No. 1062 of August 10, 2021. R.K. acknowledges the financial support from the MUT University Grant UGB 22 804 from funds for year 2023.
Open Access Funding provided by Universita della Calabria within the CRUI-CARE Agreement.

Conflict of Interest

The authors declare no conflict of interest.

Data Availability Statement

The data that support the findings of this study are openly available in Zenodo at https://doi.org/10.5281/zenodo.7428783.

Keywords

Fano-Feshbach resonances, metamaterials, metasurfaces, plasmonics, metasensors

Received: December 28, 2022
Revised: February 24, 2023
Published online:

[1] P. Offermans, M. C. Schaafsma, S. R. Rodriguez, Y. Zhang, M. Crego-Calama, S. H. Brongersma, J. Gómez Rivas, *ACS Nano* **2011**, *5*, 5151.
[2] Y. Ma, B. Dong, C. Lee, *Nano Convergence* **2020**, *7*, 12.
[3] F. Yesilkoy, *Sensors* **2019**, *19*, 4287.
[4] Y.-Y. Luk, M. L. Tingey, D. J. Hall, B. A. Israel, C. J. Murphy, P. J. Bertics, N. L. Abbott, *Langmuir* **2003**, *19*, 1671.
[5] Z. Jing, P. Yu, A. Movsesyan, C. Ma, P. Li, Y. Zhu, A. O. Govorov, A. Neogi, Z. Wang, *Adv. Opt. Mater.* **2022**, *10*, 2201066.
[6] A. Movsesyan, L. V. Besteiro, X.-T. Kong, Z. Wang, A. O. Govorov, *Adv. Opt. Mater.* **2022**, *10*, 2101943.
[7] B. Luk'yanchuk, N. I. Zheludev, S. A. Maier, N. J. Halas, P. Nordlander, H. Giessen, C. T. Chong, *Nat. Mater.* **2010**, *9*, 707.
[8] V. G. Kravets, A. V. Kabashin, W. L. Barnes, A. N. Grigorenko, *Chem. Rev.* **2018**, *118*, 5912.
[9] A. D. Utyushev, V. I. Zakomirnyi, I. L. Rasskazov, *Rev. Phys.* **2021**, *6*, 100051.
[10] N. Papasimakis, N. I. Zheludev, *Opt. Photonics News* **2009**, *20*, 22.
[11] Z. Han, S. I. Bozhevolnyi, *Opt. Express* **2011**, *19*, 3251.
[12] B. Dana, A. Bahabad, *Opt. Express* **2016**, *24*, 22334.
[13] G. E. Lio, A. Ferraro, M. Giocondo, R. Caputo, A. De Luca, *Adv. Opt. Mater.* **2020**, *8*, 2000487.
[14] A. Ferraro, G. E. Lio, M. D. L. Bruno, S. Nocentini, M. P. De Santo, D. S. Wiersma, F. Riboli, R. Caputo, R. C. Barberi, *Adv. Mater. Technol.* **2022**, *8*, 2201010.
[15] J.-P. Connerade, A. Lane, *Rep. Prog. Phys.* **1988**, *51*, 1439.
[16] A. A. Sukhorukov, A. S. Solntsev, S. S. Kruk, D. N. Neshev, Y. S. Kivshar, *Opt. Lett.* **2014**, *39*, 462.
[17] M. F. Limonov, M. V. Rybin, A. N. Poddubny, Y. S. Kivshar, *Nat. Photonics* **2017**, *11*, 543.
[18] A. Poddubny, I. Iorsh, P. Belov, Y. Kivshar, *Nat. Photonics* **2013**, *7*, 948.
[19] G. E. Lio, G. Palermo, R. Caputo, A. De Luca, *RSC Adv.* **2019**, *9*, 21429.
[20] W. Wang, L. V. Besteiro, P. Yu, F. Lin, A. O. Govorov, H. Xu, Z. Wang, *Nanophotonics* **2021**, *10*, 1911.
[21] E. Economou, *Phys. Rev.* **1969**, *182*, 539.
[22] C. L. Smith, N. Stenger, A. Kristensen, N. A. Mortensen, S. I. Bozhevolnyi, *Nanoscale* **2015**, *7*, 9355.
[23] Z. Jing, P. Li, C. Ma, J. Wang, R. Caputo, A. O. Govorov, A. Neogi, H. Xu, Z. Wang, *Photonics Res.* **2022**, *10*, 2642.
[24] G. E. Lio, A. Ferraro, T. Ritacco, D. M. Aceti, A. De Luca, M. Giocondo, R. Caputo, *Adv. Mater.* **2021**, *33*, 2008644.
[25] J. Dionne, L. Sweatlock, H. Atwater, A. Polman, *Phys. Rev. B* **2005**, *72*, 075405.
[26] J. P. Hugonin, P. Lalanne, *arXiv:2101.00901*, **2021**.
[27] O. Ávalos-Ovando, L. V. Besteiro, Z. Wang, A. O. Govorov, *Nanophotonics* **2020**, *9*, 3587.
[28] D.-J. Cai, Y.-H. Huang, W.-J. Wang, W.-B. Ji, J.-D. Chen, Z.-H. Chen, S.-D. Liu, *J. Phys. Chem. C* **2015**, *119*, 4252.
[29] K. V. Sreekanth, A. De Luca, G. Strangi, *Sci. Rep.* **2013**, *3*, 3291.
[30] G. Palermo, K. V. Sreekanth, N. Maccaferri, G. E. Lio, G. Nicoletta, F. De Angelis, M. Hinczewski, G. Strangi, *Nanophotonics* **2021**, *10*, 295.
[31] G. Palermo, G. E. Lio, M. Esposito, L. Ricciardi, M. Manoccio, V. Tasco, A. Passaseo, A. De Luca, G. Strangi, *ACS Appl. Mater. Interfaces* **2020**, *12*, 30181.
[32] A. V. Kabashin, P. Evans, S. Pastkovsky, W. Hendren, G. A. Wurtz, R. Atkinson, R. Pollard, V. A. Podolskiy, A. V. Zayats, *Nat. Mater.* **2009**, *8*, 867.
[33] S.-F. Lin, C.-M. Wang, T.-J. Ding, Y.-L. Tsai, T.-H. Yang, W.-Y. Chen, J.-Y. Chang, *Opt. Express* **2012**, *20*, 14584.
[34] M. Yang, X. Xiong, R. He, Y. Luo, J. Tang, J. Dong, H. Lu, J. Yu, H. Guan, J. Zhang, Z. Chen, M. Liu, *ACS Appl. Mater. Interfaces* **2018**, *10*, 5933.
[35] A. Manolis, E. Chatzianagnostou, G. Dabos, N. Pleros, B. Chmielak, A. Giesecke, C. Porschatis, P. Cegielski, L. Markey, J.-C. Weeber, A. Dereux, D. Tsiokos, *Opt. Express* **2019**, *27*, 17102.
[36] S. Joseph, S. Sarkar, J. Joseph, *ACS Appl. Mater. Interfaces* **2020**, *12*, 46519.
[37] D. N. Maksimov, V. S. Gerasimov, A. A. Bogdanov, S. P. Polyutov, *Phys. Rev. A* **2022**, *105*, 033518.
[38] L. Qian, T. Gu, S. Xu, X. Zhang, K. Wang, *Opt. Express* **2023**, *31*, 1844.
[39] A. Ferraro, G. E. Lio, A. Hmina, G. Palermo, J. M. Djouda, T. Maurer, R. Caputo, *Nanophotonics* **2021**, *10*, 3907.
[40] Y. Li, S. Park, M. McLamb, M. Lata, S. Schöche, D. Childers, I. Aggarwal, M. Poutous, G. Boreman, T. Hofmann, *Opt. Mater. Express* **2019**, *9*, 4318.
[41] M. Schmid, D. Ludescher, H. Giessen, *Opt. Mater. Express* **2019**, *9*, 4564.